J Mater Sci

Ceramics

Effects of boron doping and pre-heat treatment on the stabilization of tetragonal zirconia in sol-gel-derived ZrO_2–SiO_2 glass–ceramics

Yusuf Çelik[1], Ahmet Furkan Buluç[2], Servet Turan[2,3], Ali Erçin Ersundu[1], and Miray Çelikbilek Ersundu[1,*]

[1] *Faculty of Chemical and Metallurgical Engineering, Department of Metallurgical and Materials Engineering, Glass Research and Development Laboratory, Yildiz Technical University, 34220 Istanbul, Türkiye*

[2] *Ceramic Research Center, Eskisehir Technical University Iki Eylul Campus Tepebasi, 26555 Eskisehir, Türkiye*

[3] *Faculty of Engineering, Department of Materials Science and Engineering, Eskisehir Technical University, 26480 Eskisehir, Türkiye*

Received: 26 November 2025
Accepted: 16 February 2026

© The Author(s), 2026

ABSTRACT

The long-term performance of zirconia-based glass–ceramics in structural applications, such as restorative dentistry, depends on phase stability, controlled microstructure, and optimized mechanical properties. This study systematically examines the effects of boron doping and pre-heat treatment on the phase evolution, microstructure, and hardness of sol-gel-derived ZrO_2–SiO_2 glass–ceramics. Xerogel powders containing boron (1–4 mol%) were pre-treated at 650–1000 °C and consolidated by spark plasma sintering. Boron addition promoted tetragonal ZrO_2 stabilization, while pre-heat treatment enabled controlled crystallization and grain growth. The 2 mol% boron-doped sample showed the highest hardness (7.88 GPa), ~ 6% higher than the undoped composition at 900 °C. Excessive boron addition at higher temperatures slightly reduced hardness due to lower density. Moderate boron doping effectively stabilizes tetragonal zirconia and tailors microstructure through a simple, scalable, and cost-efficient route, offering a promising strategy for high-performance zirconia-based glass–ceramics in structural and dental applications.

Introduction

In restorative dentistry, selecting materials with appropriate mechanical and optical properties remains one of the most critical factors for achieving long-term clinical success. This requirement strongly links dentistry and materials science, as advances in one directly influence the progress of the other [1]. Dental materials are generally classified as metallic, ceramic, polymeric, or composite materials, each possessing specific advantages and limitations depending on their chemical structure and intended clinical use [1, 2]. Among these, dental ceramics have gained significant

Handling Editor: Andréa de Camargo.

Address correspondence to E-mail: miray@yildiz.edu.tr

https://doi.org/10.1007/s10853-026-12452-1
Published online: 03 March 2026

attention due to their excellent biocompatibility, esthetic appearance, and favorable mechanical properties such as hardness, wear resistance, and chemical durability [2, 3].

Zirconia-based ceramics are particularly prominent in dental applications due to their exceptional mechanical reliability and resistance to degradation [4, 5]. Among its polymorphs (monoclinic, tetragonal, and cubic), the tetragonal phase is especially valued for its superior combination of strength, toughness, and durability [4, 5]. Stabilizing the high-temperature tetragonal phase at room temperature is thus crucial to performance. In particular, partially stabilized zirconia and tetragonal zirconia polycrystals are widely used in dental applications, benefiting from transformation toughening and mechanical robustness [4, 6, 7]. However, conventional sintering often leads to grain coarsening and phase instability, limiting optical properties and long-term reliability [7, 8].

To overcome these challenges, ZrO_2–SiO_2 glass–ceramic systems have been investigated as their amorphous matrices enable controlled crystallization and tunable mechanical/optical properties [9–13]. Reported synthesis methods include wet chemical routes [14], oxalate processing [15], sol-gel and its modifications [16–18], as well as hybrid sol–sol approaches [19]. Nevertheless, most studies emphasize silica-rich compositions, while zirconia-rich systems—critical for maximizing tetragonal content—remain less explored. Only a few works report nanoscale particle sizes (5–40 nm) from sol-gel processing [16]. Melt-quenching has also been attempted, but the tetragonal fraction rarely exceeded ~ 52% and decreased upon heat treatment [20].

Given these limitations, the sol-gel technique was chosen in this study for its molecular-level homogeneity, uniform oxide dispersion, and precise stoichiometric control, combined with low-temperature processing advantages [12, 13, 21–23]. In ZrO_2–SiO_2 system, increasing ZrO_2 enhances mechanical strength by promoting crystallinity, but reduces glass-forming ability, making processing challenging. Higher SiO_2 favors better glass stability and crystallization control, producing finer grains [10, 11, 13]. Based on the phase diagram and glass-forming ability map, a composition of 35 mol% SiO_2–65 mol% ZrO_2 was selected, as it falls within a region where tetragonal ZrO_2 is thermodynamically stable and can coexist with $ZrSiO_4$, enabling selective crystallization [11–13, 24, 25].

While composition plays a central role in controlling crystallization, dopant incorporation is another strategy to influence crystallization and phase stability in ZrO_2–SiO_2 glass–ceramics. Yttria (Y_2O_3) is the most effective stabilizer, improving densification and retaining the tetragonal phase even at larger grain sizes [26–28]. Other dopants such as Al and Ca tend to segregate at ZrO_2/SiO_2 interfaces, affecting coarsening, while Ta, Nb, and Hf have been shown to destabilize tetragonal ZrO_2 and induce coloration [29, 30]. Most additives, however, mainly strengthen the SiO_2 glassy matrix rather than effectively stabilizing tetragonal ZrO_2 [30, 31]. A further key factor is crystallite size: Tetragonal ZrO_2 remains stable only below a critical threshold (~ 50 nm in ZrO_2–SiO_2 systems [32] and ~ 30 nm in pure ZrO_2 [33]). This highlights the importance of processing routes that refine microstructure and control crystallization to preserve tetragonal stability.

In this context, boron—typically introduced via boric acid in sol-gel synthesis—has been shown in other oxide systems to act both as a glass network modifier and as a low-level dopant affecting phase evolution and grain boundary behavior [34–36]. With its small ionic radius and high mobility, B^{3+} promotes densification, reduces crystallization temperature, and can stabilize metastable phases [35, 36]. To the best of our knowledge, boron incorporation has not been explored in ZrO_2–SiO_2 glass–ceramics, representing a novel approach to stabilizing tetragonal ZrO_2 while tailoring microstructure and optical properties.

Therefore, this study aims to synthesize undoped and B-doped ZrO_2–SiO_2 glass–ceramics via sol-gel processing followed by spark plasma sintering (SPS), investigating the combined effects of boron addition and tailored sintering on phase evolution, microstructure, and mechanical/optical performance. To promote controlled crystallization and suppress grain growth, a series of thermal pre-treatments was introduced prior to SPS to favor nanoscale tetragonal retention and eliminate residual carbon from sol-gel precursors. The most effective conditions were then applied to B-doped compositions. This dual strategy—introducing boron as a novel stabilizing additive and applying pre-SPS thermal engineering—constitutes the central novelty of the work, offering new pathways

for the design of advanced zirconia-based dental ceramics.

Experimental

Preparation and optimization of ZrO_2–SiO_2 sol-gel-derived Nanopowders

ZrO_2–SiO_2 glass–ceramics were synthesized via the sol-gel method using zirconium n-propoxide $Zr(OPr)_4$, 70 wt% in 1-propanol, Sigma-Aldrich) and tetraethyl orthosilicate (TEOS, 98%, Sigma-Aldrich) as the primary precursors. Hydrolysis and polycondensation reactions were carefully controlled to ensure molecular-level homogeneity and prevent premature precipitation. Solution 1 was prepared by mixing zirconium n-propoxide with 1-propanol under magnetic stirring for 2 h in a sealed container to minimize moisture interference, while Solution 2 was obtained by dissolving TEOS in ethanol and acidifying with 0.4 M HCl, followed by 2 h of stirring to initiate partial hydrolysis. For B-doped samples, boric acid (H_3BO_3) was incorporated into the TEOS-based sol prior to gelation at concentrations of 1–4 mol% relative to the total oxide content and thoroughly dissolved to ensure homogeneous distribution. The two precursor solutions were then combined under vigorous stirring and homogenized for an additional 2 h to form a clear, stable sol. Gelation was induced by adding concentrated HCl (12 M, 37% fuming) dropwise using a 1-mL pipette under strong stirring. A total of 15 mL HCl per 100 mL sol was added gradually over 8 h (1 mL every 30 min) to avoid formation of white zirconia-rich precipitates. Wet gels were aged at 60 °C for 7 days, dried at 120 °C for 24 h to obtain xerogels, and manually crushed and ground to reduce particle size. Digital photographs of selected undoped and B-doped sols and xerogels are shown in Figure S1.

To optimize the sol-gel composition, the effects of HCl, 1-propanol, and zirconium n-propoxide on gelation and process stability were systematically investigated. Small variations in acid quantity triggered premature gelation, while adjusting solvent content and accounting for zirconium loss allowed precise control. Scaled-up experiments confirmed that a molar ratio of $Zr(OPr)_4$:1-propanol:HCl = 4:10:0.32 provided optimal gelation time, process stability, and sol homogeneity (Figure S2, Table S1).

To remove residual organics and promote phase development, an initial two-step heat treatment strategy, consisting of calcination and crystallization, was applied. In line with common literature practice, xerogels were first calcined at 600 °C for 1 h with a ramp rate of 1 °C/min. This pre-SPS treatment is widely used to remove carbonaceous residues, but in our case, the resulting dark-gray powders indicated incomplete organic removal. Therefore, a single-step higher-temperature treatment was adopted to simultaneously achieve calcination and crystallization. Based on literature guidance and experimental optimization (Figure S3), three pre-heat treatment protocols were selected: (i) 650 °C for 1 h, (ii) 900 °C for 15 min, and (iii) 1000 °C for 5 min. Conditions (ii) and (iii) were specifically intended to simultaneously remove residual carbon, promote tetragonal phase formation, and control grain growth in the ZrO_2–SiO_2 system. An overview of the experimental procedure is illustrated in Fig. 1.

Spark plasma sintering studies

To densify the samples while minimizing undesirable grain growth beyond the critical size of tetragonal zirconia crystals, SPS was employed. Prior to finalizing the sintering conditions, a literature survey of ZrO_2–SiO_2 and related oxide ceramics was conducted, with attention to reported correlations between holding temperature, applied pressure, dwell time, and resulting properties (e.g., transmittance, microhardness, biaxial flexural strength, apparent and relative density, and crystallite size). Based on these insights, the sintering parameters were selected to achieve high densification while preserving nanoscale grain sizes [12, 13, 28].

Approximately 6 g of powder was loaded into a 20-mm graphite die. To prevent reactions with the die and current flow, the inner surfaces were lined with graphite foil and the assembly insulated with a graphite felt blanket. A preliminary uniaxial pressure of 40 MPa was manually applied for 30 s before placing the die into the SPS chamber (FCT Systems FAST/SPS HP D 25/1). After evacuation, a maximum uniaxial pressure of 50 MPa was applied throughout the process.

Heating was carried out in two stages: (i) from room temperature to 900 °C at 120 °C/min, with a 2-min dwell to promote initial densification and eliminate larger interparticle voids, and (ii) from 900 °C to

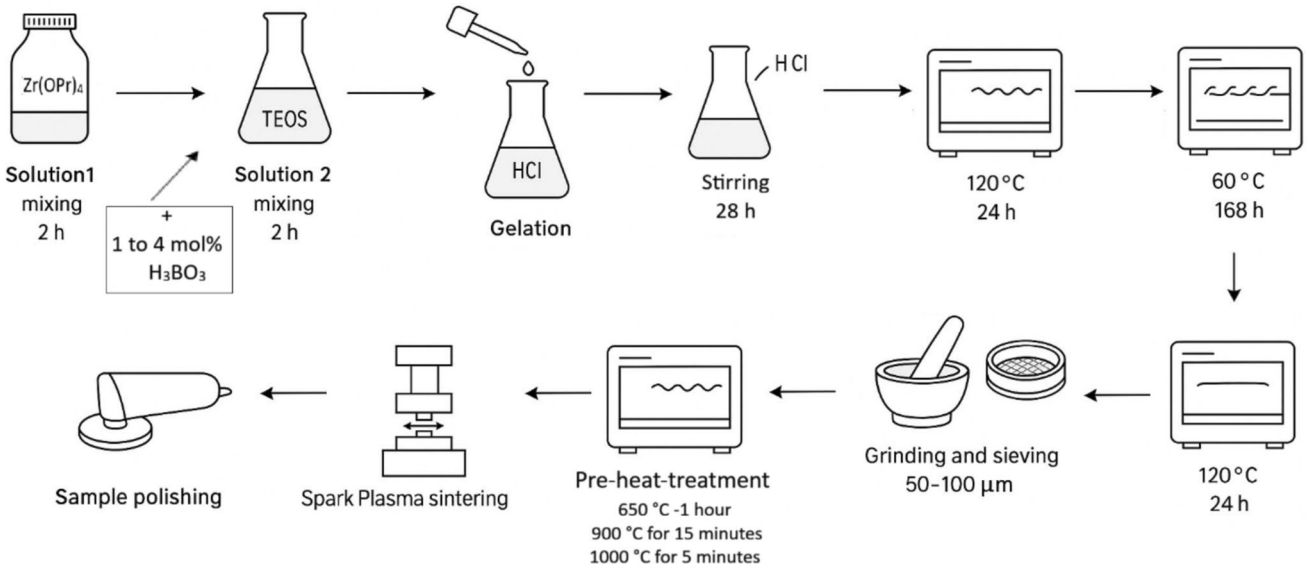


Figure 1 Experimental workflow for the sol-gel synthesis of ZrO_2–SiO_2 powders (undoped and B-doped), including pre-heat treatment and SPS processing.

the target sintering temperature at 30 °C/min. The temperature was determined by monitoring the piston movement during sintering, and a dwell time of 5 min was given for sintering at the determined temperature. Heating switched off, and the samples were rapidly cooled under vacuum to preserve nanocrystallinity.

Following SPS, samples were mechanically polished to remove surface graphite residues. Polishing involved sequential wet grinding with SiC papers (120#–2500#), followed by final polishing with a 1 µm diamond suspension on an automatic polisher (Struers LaboPol-20). Representative digital photographs of sintered samples are shown in Fig. 2.

Characterization studies

The chemical composition of the xerogels was verified using energy-dispersive X-ray fluorescence (ED-XRF, Malvern PANalytical Epsilon 4) to confirm

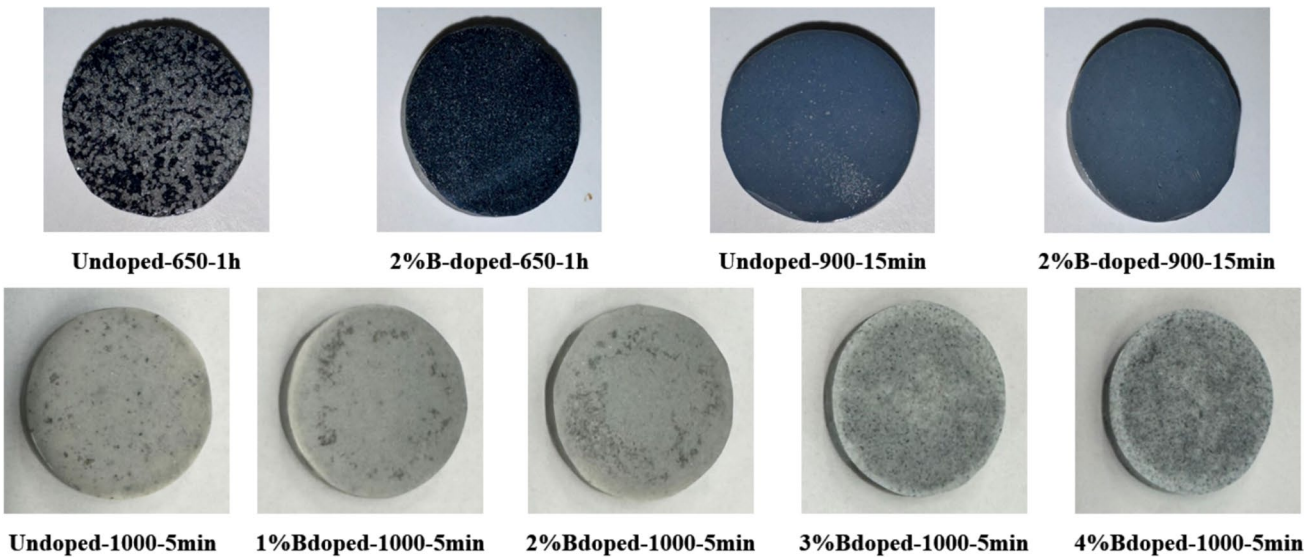


Figure 2 Digital photographs of sintered undoped and B-doped samples under three different pre-heat treatment conditions.

that the targeted stoichiometry was preserved after sol-gel synthesis and drying.

Thermal analyses of selected amorphous powders were performed using thermogravimetric and differential scanning calorimetry (Netzsch STA 449 F3 Jupiter) to evaluate their thermal behavior prior to heat treatment. Approximately 30 ± 1 mg of powder was placed in alumina pans and heated from room temperature to 1200 °C at 10 °C/min under a nitrogen flow of 50 mL/min. These measurements allowed identification of solvent evaporation, organic decomposition, mass stabilization, and the onset of zirconia crystallization.

The phase composition and crystallinity of both powders and sintered samples were assessed by X-ray powder diffraction (XRD) using a Malvern PANalytical Empyrean MultiCore diffractometer. Crystallite sizes of zirconia were estimated from the diffraction patterns via the Debye–Scherrer equation:

$$\tau = \frac{K\lambda}{\beta cos\theta}\# \quad (1)$$

where τ is the crystallite size, λ is the X-ray wavelength, θ is the diffraction angle, and β is the full width at half maximum (FWHM) of the peak. Rietveld refinement was applied to quantify the crystalline zirconia fraction within the amorphous silica matrix.

Densities (ϱ) of sintered samples were measured at room temperature using Archimedes' principle with deionized water as the immersion medium. A Precisa XB 220A digital balance (± 10^{-4} g) was used, with five measurements per sample with a maximum error of ± 1%. Density was calculated as:

$$\rho = \rho_{liquid}\frac{W_{air}}{W_{air}-W_{liquid}}\# \quad (2)$$

where W_{air} and W_{liquid} are the weights of the sample in air and in deionized water, respectively.

Fourier transform infrared spectroscopy (FTIR) spectroscopy (Perkin-Elmer Spectrum 100) was used to probe bonding and functional group structures. Amorphous powders were analyzed using the KBr pellet method, whereas sintered samples were examined in attenuated total reflectance (ATR) mode to monitor structural changes induced by heat treatment and densification.

Mechanical properties were evaluated via Vickers microhardness measurements using a DHV-1000(Z) tester. Loads ranging from 10 to 200 gf were applied for 10 s per indentation, and indentation diagonals were measured with a CCD-equipped optical microscope and image analysis software. Ten non-overlapping indentations were performed per sample, and average values were reported.

Finally, microstructural and elemental analyses were carried out using field emission scanning electron microscopy (FESEM) combined with energy-dispersive X-ray spectroscopy (EDS) on a Thermo Scientific Apreo 2 S LoVac instrument. Polished surfaces of sintered samples were etched with HF for 1 min to enhance grain boundary contrast. FESEM and EDS enabled visualization of grain morphology, size distribution, and qualitative elemental mapping of silicon, zirconium, and oxygen.

Results and discussion

Non-sintered samples

XRF analyses were performed on the non-sintered sol-gel-derived powders (nominal composition: 65 mol% ZrO_2 / 35 mol% SiO_2, equivalent to 79.2 wt% / 20.8 wt%). Measurements under both air and He atmospheres confirmed minimal deviation from the target composition, indicating that the sol-gel process effectively preserved the intended stoichiometry. Representative values were 78.38 wt% ZrO_2, 19.23 wt% SiO_2, and 2.39 wt% Cl, with the minor chlorine content attributed to residual chlorides from the precursors.

With the stoichiometry confirmed by XRF, the powders' thermal behavior was next evaluated by STA to assess solvent evaporation, organic decomposition, and zirconia crystallization. Analyses were performed on both undoped and B-doped amorphous powders, i.e., xerogels obtained from dried gels, to identify critical temperatures for the transition of dried gels into glassy or crystalline phases. The STA results for the undoped and 2 mol% B-doped samples are shown in Fig. 3, highlighting the effect of boron on thermal decomposition.

The analysis revealed three distinct stages of mass loss, totaling ~ 24%, after which the powders exhibited thermal stability above 800 °C. The first stage, below 400 °C, occurred in two overlapping steps corresponding to desorption of physically adsorbed water and residual alcohols (~ 100 °C) and removal of organic groups with partial dehydroxylation (~ 250 °C). A third, minor weight loss around 700–800 °C was attributed to elimination of remaining hydroxyl

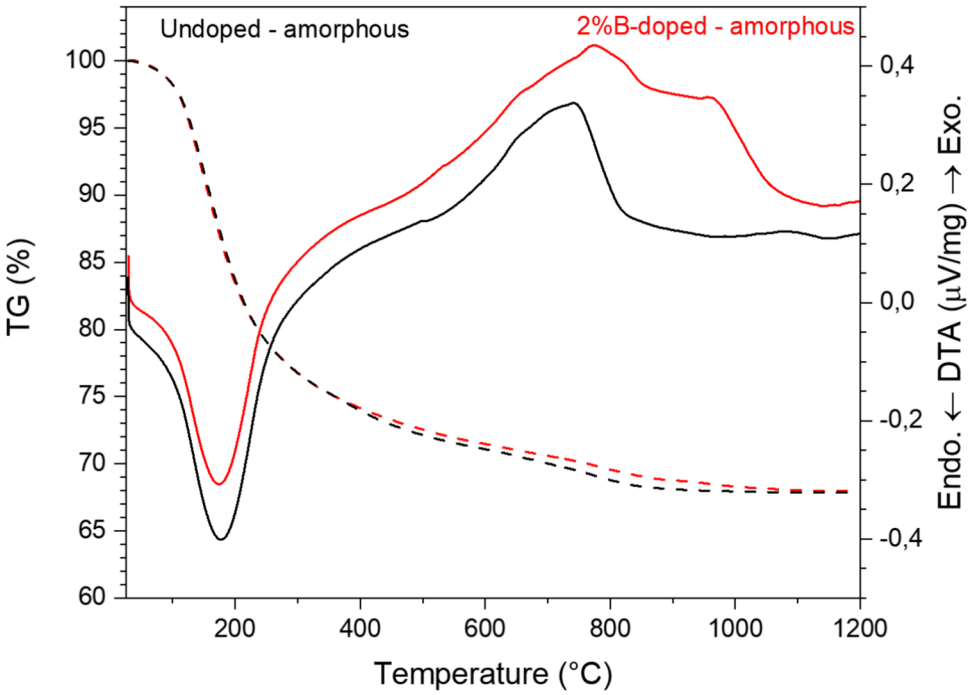


Figure 3 TG/DTA curves of undoped and 2 mol% B-doped ZrO_2–SiO_2 xerogels, showing mass loss steps and the influence of boron on thermal decomposition. Dashed lines represent TG curves, while solid lines correspond to DTA signals

groups. Beyond this point, the residual mass remained constant, indicating the formation of a thermally stable inorganic framework. Notably, boron addition slightly shifted the decomposition events, suggesting modifications to the network structure and improved thermal stability that could affect subsequent crystallization.

In undoped amorphous samples, the tetragonal-to-monoclinic transformation typically begins near 500 °C and is completed between 800 and 950 °C [16]. However, in sol-gel-derived zirconia, crystallization of the tetragonal phase has been reported at much lower temperatures (~ 300 °C) due to microcrystalline domain formation and process-specific conditions [37]. In the present study, B doping delayed this transformation, with the onset around 500 °C but completion only above 1050 °C. These results demonstrate that boron incorporation enhances tetragonal phase stability, an important factor for achieving high-performance microstructures during SPS processing.

To investigate the bonding characteristics of the undoped and B-doped xerogels, FTIR spectra were recorded (Fig. 4), revealing four characteristic absorption bands near 3200, 1620, 1050, and 590 cm^{-1}. The broad band around 3200 cm^{-1}corresponds to –OH stretching and bending vibrations from adsorbed water or surface hydroxyl groups, while the band near 1620 cm^{-1} is assigned to the bending

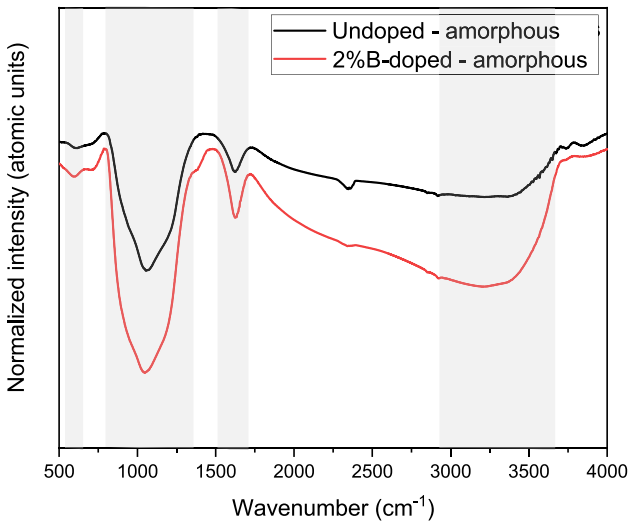


Figure 4 FTIR spectra of sol-gel synthesized undoped and 2% B-doped xerogels, showing characteristic absorption bands associated with hydroxyl groups, silicate/borosilicate linkages, and zirconia vibrations.

vibration of molecular water (H–O–H). The strong band at ~ 1050 cm^{-1} arises from asymmetric stretching vibrations of Si–O–Si and B–O–Si linkages, and its more pronounced and broadened spectral feature in the B-doped sample suggests the formation

of borosilicate linkages and a modified network connectivity.

In the 650–550 cm^{-1} range, a band associated with Zr–O–Zr vibrations is observed, with the peak shifting from 590 to ~ 600 cm^{-1} upon B doping. This shift, along with the appearance of a small additional peak near 750 cm^{-1}, suggests possible Zr–B bonding interactions and modification of the local zirconia environment [38–41].

These boron-induced structural modifications are expected to influence the crystallization pathway of ZrO_2 during subsequent heat treatment. In particular, B–Si and B–Zr interactions may enhance structural disorder and restrict long-range diffusion, thereby suppressing excessive grain growth and stabilizing the tetragonal ZrO_2 phase against monoclinic transformation. This interpretation is consistent with the observed FTIR features and supported by literature reports on the stabilizing role of boron in zirconia-containing glass–ceramic systems [35, 36].

Based on STA results and literature data on phase transitions in sol-gel-derived ZrO_2, three representative heat treatment protocols were selected: (i) 650 °C for 1 h, (ii) 900 °C for 15 min, and (iii) 1000 °C for 5 min. These conditions were designed to eliminate residual organics, induce controlled crystallization, and stabilize the metastable tetragonal phase. The crystalline phases obtained after heat treatment were subsequently examined by XRD. Figure 5 shows the diffraction patterns of undoped and 2 mol% B-doped samples, together with reference patterns for tetragonal ZrO_2 (ICDD #04–013-6619) and monoclinic ZrO_2 (ICDD #00–065-0687).

XRD results confirmed that all heat-treated samples, both undoped and B-doped, exhibited exclusively the tetragonal ZrO_2 phase, with no evidence of monoclinic transformation or secondary phases. This demonstrates that the sol-gel-derived amorphous precursors successfully crystallized into the desired tetragonal structure upon thermal treatment, highlighting the effectiveness of the synthesis and heat treatment protocol in controlling phase formation.

To quantify the crystalline content, Rietveld refinements were performed to estimate the fraction of crystallized zirconia within the amorphous silica matrix. Figure 6 presents the refinement results for the undoped and 2 mol% B-doped samples heat-treated at 900 °C for 15 min. Both samples only consisted of the targeted tetragonal phase, with no secondary phases detected. The refinements yielded χ^2 values of 1.23

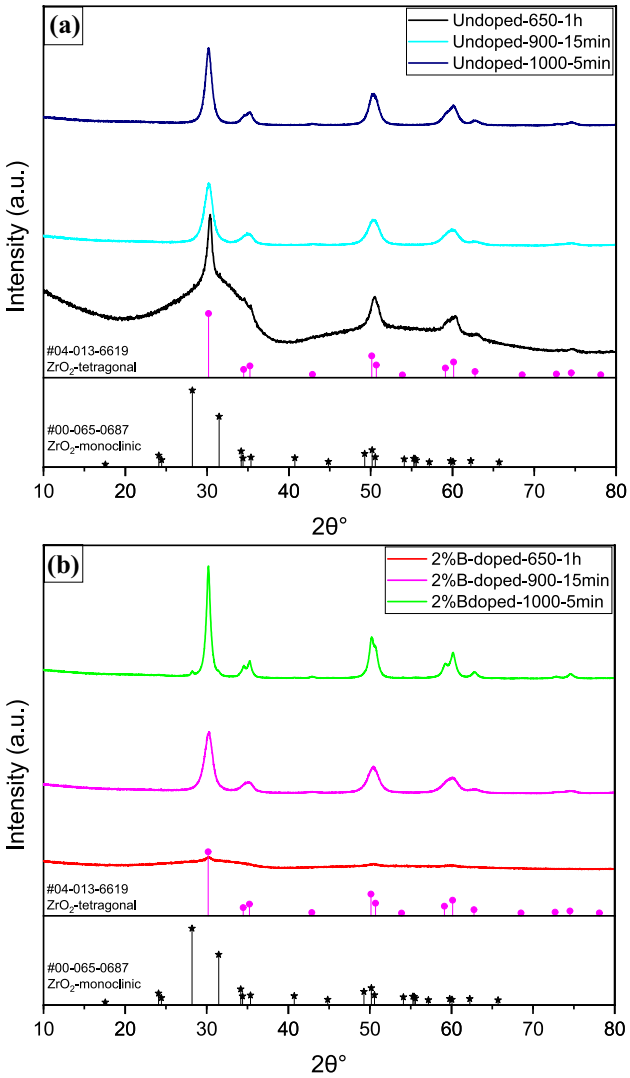


Figure 5 XRD patterns of (**a**) undoped and (**b**) 2 mol% B-doped powders after heat treatments at 650 °C, 900 °C, and 1000 °C, showing the formation of tetragonal and monoclinic ZrO_2 phases.

and 1.17, respectively, and R-factors of 6.35 and 5.98, confirming a good fit between observed and calculated diffraction patterns. Lattice parameters matched reference data, validating the phase identification. Peak positions and intensities further indicate well-crystallized structures with minimal lattice strain or defects. Overall, Rietveld analysis confirms that the crystallized zirconia in both samples is overwhelmingly tetragonal.

Average crystallite sizes of zirconia were calculated from the XRD patterns using the Debye–Scherrer equation ($\lambda = 0.15406$ nm, $K = 0.89$). The results, along

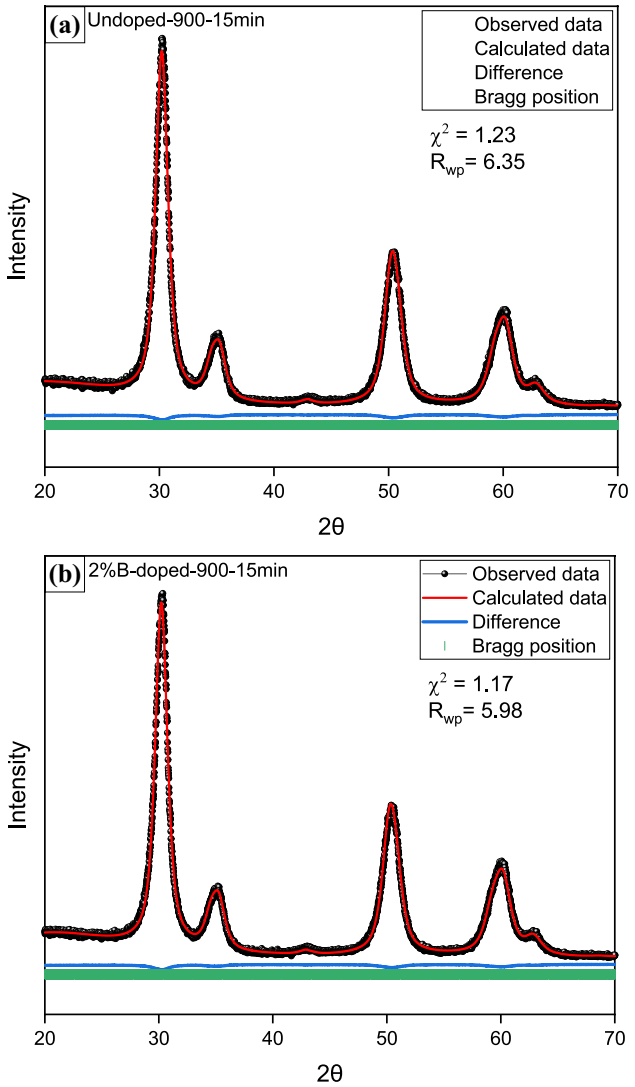


Figure 6 Rietveld refinement of (**a**) undoped and (**b**) 2 mol% B-doped ZrO_2–SiO_2 powders heat-treated at 900 °C for 15 min.

with the powders' visual color characteristics, are summarized in Table 1.

The calculated crystallite sizes ranged between ~ 9 nm and 25 nm, confirming that all samples fall within the nanocrystalline regime. At the lower temperature (650 °C, 1 h), the XRD patterns were highly amorphous, preventing reliable peak resolution and thus precluding crystallite size determination. At higher temperatures (900–1000 °C), the amorphous fraction diminished, and the B-doped samples displayed larger crystallite sizes than their undoped counterparts, indicating that boron may enhance grain boundary mobility or lower the activation barrier for grain growth. Overall, the results indicate that boron promotes crystallite growth at elevated temperatures, while tetragonal ZrO_2 persists as the sole crystalline phase under all conditions.

To investigate particle size, morphology, and microstructural features, FESEM analyses were performed on the undoped sample heat-treated at 900 °C for 15 min (Fig. 7). Low-magnification images (Fig. 7a) revealed agglomerated ZrO_2 nanoparticles with a broad particle size distribution. A closer view of a selected region (Fig. 7b) was used for elemental mapping (Figs. 7c–g), confirming that the bright grains correspond to ZrO_2 crystallites, while the darker background arises from the amorphous ZrO_2–SiO_2 matrix and the carbon tape used during analysis. At higher magnification (Figs. 7h and i), individual ZrO_2 grains with average diameters of ~ 15 nm were observed, in good agreement with crystallite sizes estimated from XRD via the Debye–Scherrer equation. This correlation further supports the nanostructured nature of the synthesized powders.

Table 1 Average crystallite size (τ), full width at half-maximum (FWHM, β), Bragg angle (θ), and visual color of the powders, calculated from XRD data using the Debye–Scherrer equation

Sample Name	Av. crystallite size, τ	FWHM, β		θ	Powder color
	nm	degree	radian	degree	
Undoped-650-1 h	–	–	–	–	dark gray
2%B-doped-650-1 h	–	–	–	–	dark gray
Undoped-900-15 m	13.94	0.2047	0.0036	30.22	white
2%B-doped-900-15 m	25.49	0.1535	0.0027	30.37	light gray
Undoped-1000-5 m	9.08	0.2558	0.0045	30.15	white
2%B-doped-1000-5 m	21.08	0.1407	0.0024	30.23	white

–: values not determined due to the highly amorphous nature of the XRD patterns, which prevented reliable peak resolution

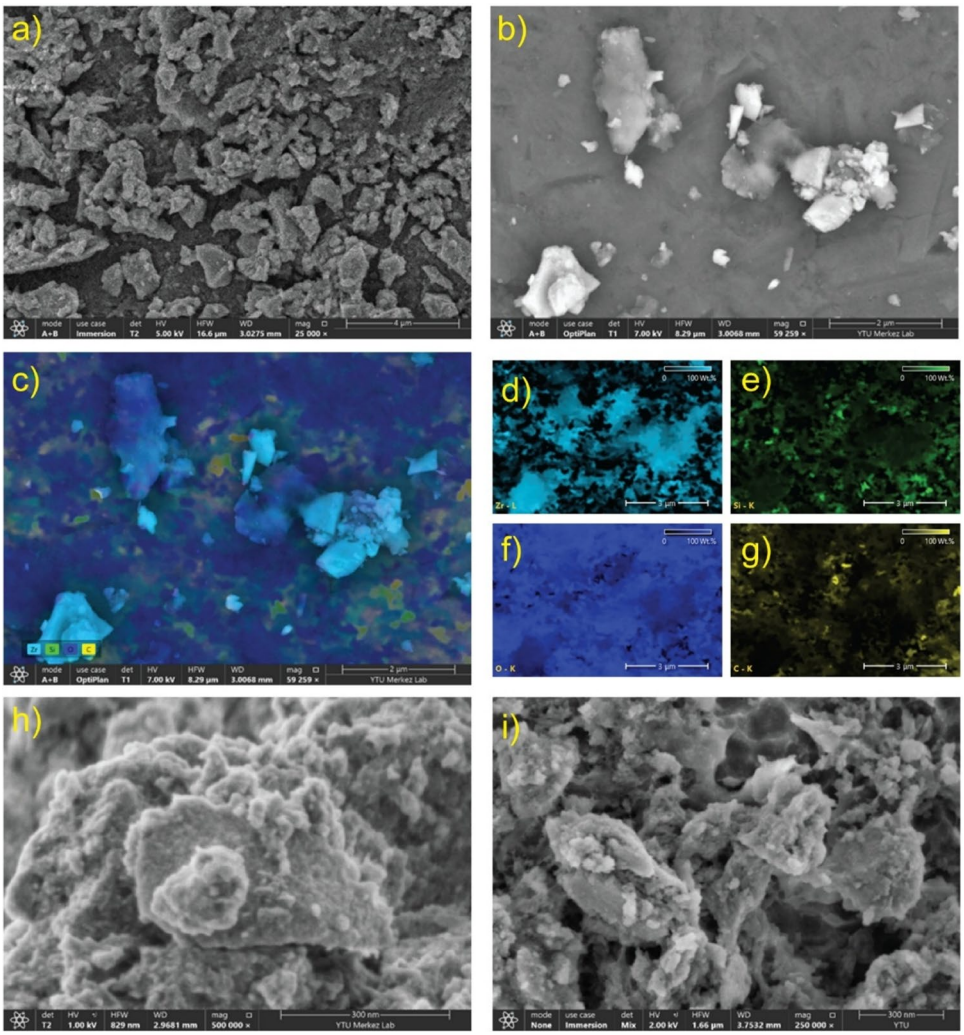


Figure 7 FESEM analysis of the undoped sample heat-treated at 900 °C for 15 min: (**a**) low-magnification image showing particle agglomeration and broad size distribution, (**b**) selected region used for elemental mapping, (**c**–**g**) EDS elemental maps of Zr, Si, O, and C, (**h**, **i**) high-magnification images revealing nanocrystalline ZrO_2 grains.

SPS-treated samples

The amorphous powders were sintered using SPS, and the subsequent analyses focused on the effects of both the pre-heat treatment conditions—(i) 650 °C for 1 h, (ii) 900 °C for 15 min, and (iii) 1000 °C for 5 min—and boron addition (1–4 mol %) on the phase composition, densification, and mechanical properties of the sintered samples. Figure 8 presents the temperature and displacement profiles recorded during SPS for all samples, while Figure S4 shows the profiles individually for each sample. The temperature curves (Fig. 8a) follow a consistent three-step heating path up to 900 °C, including a 5-min dwell, enabling direct comparison across the different sintering scenarios. The corresponding displacement curves (Fig. 8b) illustrate the densification behavior and provide indications of possible phase transitions during sintering.

As shown in Fig. 8a, increasing the pre-heat treatment temperature and adding boron shifted the SPS sintering onset to lower temperatures. Samples pre-heat-treated at 900 °C for 15 min and 1000 °C for 5 min initiated sintering earlier than those pre-heat-treated at 650 °C for 1 h, indicating that short, high-temperature pre-heat treatments promote effective densification by removing residual organics and modifying the initial microstructure. Samples enriched in the tetragonal phase exhibited lower sintering temperatures than those containing significant amorphous fractions, consistent with delayed and slower densification in the 650 °C–1 h samples, moderate improvement at 900 °C–15 min, and the earliest densification at 1000 °C–5 min samples.

Boron addition further lowered the sintering onset, with the effect depending on both B content and pre-heat treatment. At 650 °C–1 h and 900 °C–15 min, 2%

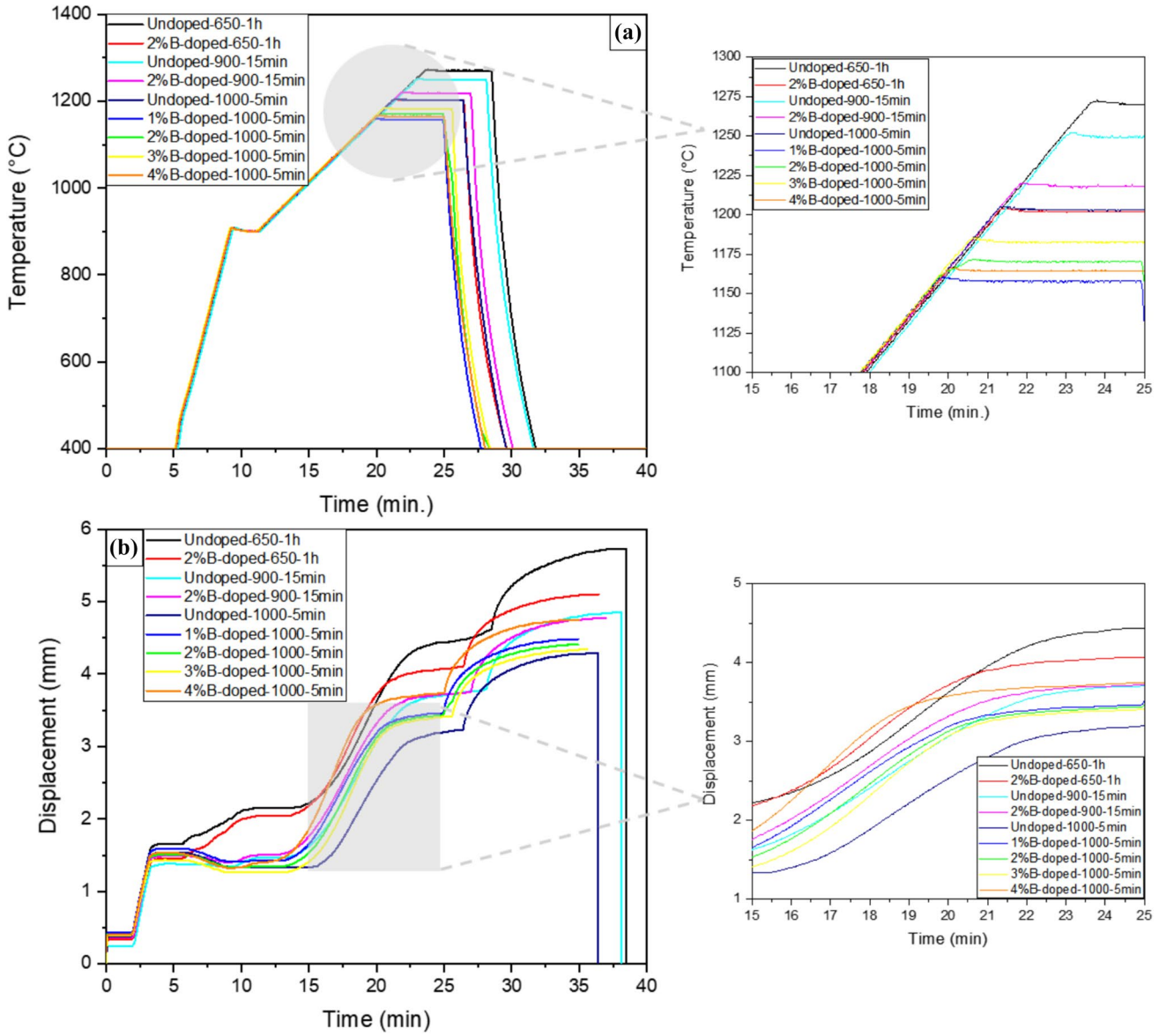


Figure 8 (**a**) Temperature–time and (**b**) displacement–time profiles recorded during SPS of undoped and B-doped samples under different sintering conditions. The curves illustrate the heating ramps, dwell stages, and densification behavior. Insets show magnified views of the high-temperature dwell region, highlighting the effect of boron content on the temperature evolution and displacement response.

B-doped samples densified earlier than undoped ones, while at 1000 °C–5 min all B-doped samples initiated sintering earlier, with the 1% B-doped sample showing the lowest onset temperature.

Displacement curves (Fig. 8b) followed a similar trend. All samples showed an initial compaction stage, but pronounced displacement was observed in 650 °C heat-treated samples due to crystallization of residual amorphous phases during SPS. With increasing pre-heat temperature, displacement decreased markedly—being limited at 900 °C and minimal at 1000 °C—reflecting suppression of crystallization-induced shrinkage. The largest displacement occurred in the undoped 650 °C sample, where zirconium silicate and mixed ZrO_2 polymorphs were present, while the smallest displacement was found in the 1000 °C sample, dominated by tetragonal ZrO_2 with negligible monoclinic content (see Fig. 9). Intermediate

displacements were consistent with mixed tetragonal–monoclinic compositions. In summary, both pre-heat treatment and boron doping strongly affect densification and phase evolution during SPS. Boron lowers the sintering onset, while pre-heat treatment governs crystallization behavior and displacement, highlighting the need to balance densification efficiency with phase stability.

Figure 9 shows the XRD patterns of the SPS-treated samples, along with reference patterns for tetragonal ZrO_2 (ICDD #04–013-6619), monoclinic ZrO_2 (ICDD #00–065-0687), and $ZrSiO_4$ (ICDD #04–007-7393). As seen in Fig. 9a, undoped samples subjected to low-temperature pre-heat treatment (650 °C, 1 h) exhibited all three phases: $ZrSiO_4$, monoclinic ZrO_2, and tetragonal ZrO_2. Increasing the pre-heat treatment temperature to 900 °C and reducing the dwell time to 15 min (Fig. 9b) decreased the intensities of $ZrSiO_4$ and monoclinic phases, while the tetragonal phase became more dominant. Further modification to 1000 °C for 5 min (Fig. 9c) eliminated detectable $ZrSiO_4$, with a significant increase in the tetragonal phase relative to monoclinic ZrO_2.

In contrast, B-doped samples predominantly consisted of the tetragonal phase, with only minor monoclinic traces, and showed complete suppression of $ZrSiO_4$ formation. A slight increase in the monoclinic-to-tetragonal ratio was observed with higher B content (Fig. 9c), emphasizing the need to optimize dopant levels. Overall, these results confirm that boron effectively suppresses $ZrSiO_4$ formation and stabilizes tetragonal ZrO_2, producing a more homogeneous tetragonal crystal structure compared to undoped samples.

The suppression of $ZrSiO_4$ formation in B-doped samples can be attributed to structural and chemical modifications introduced by B_2O_3, as well as the influence of residual carbon during sintering. Incorporation of B_2O_3 disrupts the silicate network, producing a more open glass structure with increased non-bridging oxygens, which likely reduces the mobility of Zr and Si ions and kinetically hinders $ZrSiO_4$ formation during SPS [42]. In undoped samples, particularly those pre-heat-treated at 650 °C for 1 h, ion diffusion is sufficient to promote $ZrSiO_4$ crystallization. In contrast, B-doped samples under the same conditions favor the precipitation of fine-grained tetragonal ZrO_2 crystallites. The disrupted network not only facilitates crystallization but also stabilizes the tetragonal phase by increasing the

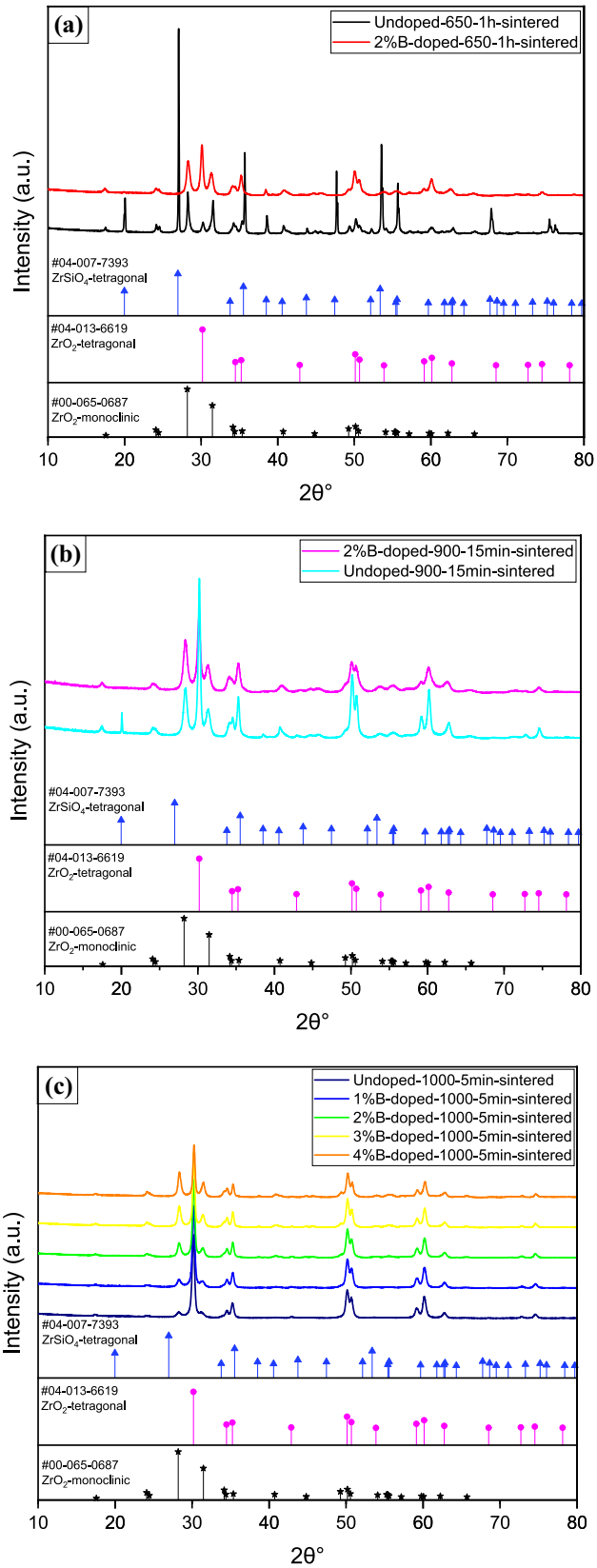


Figure 9 XRD patterns of SPS-treated undoped and B-doped samples with different pre-sintering thermal histories: (**a**) 650 °C–1 h, (**b**) 900 °C–15 min, and (**c**) 1000 °C–5 min, along with reference patterns.

temperature required for the tetragonal-to-monoclinic transformation, consistent with STA results. Additionally, incomplete carbon burnout at low pre-heat treatment temperatures may enhance local electrical conductivity during SPS, causing localized overheating and faster grain growth, which further promotes $ZrSiO_4$ formation in undoped samples. At higher pre-heat treatment temperatures (900 °C and 1000 °C), more complete carbon removal minimizes this effect.

FTIR of SPS-treated samples are presented in Fig. 10. All samples exhibit a Si–O–Zr vibration near ~ 800 cm^{-1}, indicative of $ZrSiO_4$-like environments that can hinder tetragonal ZrO_2 formation [38]. In the B-doped samples, this band shows decreased intensity, whereas the Zr–O–Zr bands at ~ 730 cm^{-1} display enhanced intensity, likely due to overlap with B–O–B bending modes [40]. In the 900–1100 cm^{-1} region, the Si–O–Si linkages become more pronounced with increasing boron addition, consistent with the inhibition of $ZrSiO_4$ crystallization and stabilization of the tetragonal phase [43]. Furthermore, a distinct band appears at ~ 1375 cm^{-1}, corresponding to the asymmetric stretching vibrations of B–O in trigonal BO_3 units [40] in B-doped samples. The presence of BO_3 units indicates that boron functions as a network former, modifying the silicate framework and disrupting Si–O–Zr linkages, thereby suppressing silicate phase formation and promoting tetragonal ZrO_2 stability. At boron levels exceeding the optimal concentration, excessive disruption of these linkages may occur, potentially compromising tetragonal stability and increasing the monoclinic fraction.

The density and hardness of the SPS-treated samples were measured to assess densification and mechanical integrity, with results summarized in Table 2 and compared to literature data for sol-gel-derived, SPS-sintered ZrO_2–SiO_2 glass–ceramics. The measured densities reflect the extent of densification achieved during SPS and are strongly influenced by both boron content and pre-sintering thermal history. The undoped sample heat-treated at 650 °C for 1 h exhibited the highest density (4.53 g/cm^3). Introducing 2 mol% boron under the same conditions led to a notable reduction in density (4.33 g/cm^3). This trend was consistent across all heat treatment regimes, demonstrating that boron doping systematically decreases the sintered density. This effect is attributed to boron-induced structural modifications, including loosening of the glass network and

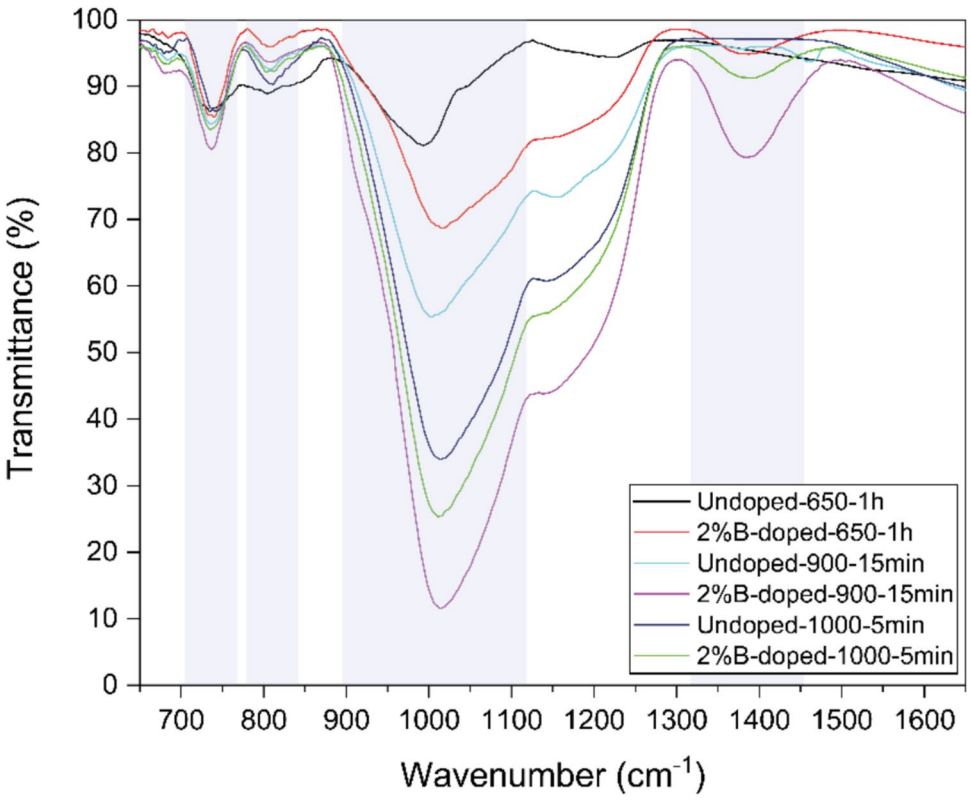


Figure 10 FTIR of SPS-treated undoped and B-doped samples after different pre-heat treatments.

Table 2 Density and Vickers hardness of SPS-sintered ZrO_2–SiO_2 glass–ceramic samples, including literature data and sintering parameters

Sample Composition	Heat treatment (°C)	Sintering Temp (°C)	Sintering Pressure (Mpa)	$\rho_{average}$ (g/cm^3)	Microhardness (GPa)	Particle Size (nm)	Ref
65Zr35Si	650-1 h	1270	50	4.53 ± 0.01	7.34 ± 0.16	53	This Study
2%B-doped-65Zr35Si	650-1 h	1200	50	4.33 ± 0.01	7.36 ± 0.21	61	
65Zr35Si	900-15 m	1250	50	4.42 ± 0.01	7.44 ± 0.03	40	
2%B-doped-65Zr35Si	900-15 m	1218	50	4.41 ± 0.01	7.88 ± 0.05	55	
65Zr35Si	1000-5 m	1203	50	4.36 ± 0.01	8.05 ± 0.03	36	
1%B-doped-65Zr35Si	1000-5 m	1160	50	4.35 ± 0.01	7.74 ± 0.04	–	
2%B-doped-65Zr35Si	1000-5 m	1171	50	4.33 ± 0.01	7.46 ± 0.01	57	
3%B-doped-65Zr35Si	1000-5 m	1183	50	4.29 ± 0.01	7.14 ± 0.04	-	
4%B-doped-65Zr35Si	1000-5 m	1165	50	4.23 ± 0.01	6.80 ± 0.04	–	
45Zr55Si	600-1 h	1150	60	3.82 ± 0.01	7.21 ± 0.10	29.5	[13]
55Zr45Si	600-1 h	1150	60	4.14 ± 0.02	7.16 ± 0.03	35.1	
65Zr35Si	600-1 h	1150	60	4.53 ± 0.03	7.57 ± 0.11	47.5	
65Zr35Si	600-1 h	1200	30	–	7.33 ± 0.2	25.4	[12]
65Zr35Si	600-1 h	1200	60	–	7.54 ± 0.1	27.9	
65Zr35Si	600-1 h	1150	60	–	7.42 ± 0.2	32.3	
5%Y-doped-65Zr35Si	600-1 h	1150	60	–	10.60	33	[29]
5%Y-doped-65Zr35Si	600-1 h	1230	40	–	–	39	[27]
70Zr30Si	600-1 h	1240	40	4.72	8.74	40.9	[31]
3%Y-doped-70Zr30Si	600-1 h	1240	40	4.76	9.40	43.2	

suppression of secondary phase formation. Additionally, boron incorporation lowers the required sintering temperature—by up to 70 °C for the sample heat-treated at 650 °C for 1 h—and sintering at reduced temperatures inherently limits densification, further contributing to the observed decrease in density. Samples pre-heat-treated at 900 °C for 15 min and 1000 °C for 5 min exhibited slightly lower densities (4.42 and 4.36 g/cm^3, respectively) than the 650 °C–1 h sample, despite higher tetragonal ZrO_2 contents. Incorporation of 2 mol% boron caused only minor additional reductions (4.41 and 4.33 g/cm^3). Although higher pre-heat treatment temperatures are typically expected to enhance densification, the opposite trend observed here is explained by phase composition. At 650 °C, the samples retained a large amorphous fraction with $ZrSiO_4$ as the dominant crystalline phase (density ≈ 4.68 g/cm^3), which raised the overall bulk density. In contrast, samples treated at 900 and 1000 °C contained little amorphous phase and were dominated by tetragonal ZrO_2. Theoretical density estimates for the 65 mol% ZrO_2–35 mol% SiO_2 system (≈4.27 g/cm^3 for monoclinic ZrO_2, ≈4.45 g/cm^3 for tetragonal ZrO_2) further support that the higher density of the 650 °C sample originates from the contribution of $ZrSiO_4$ rather than differences in porosity or incomplete sintering.

The microhardness of the undoped glass–ceramic samples ranged from 7.34 to 8.05 GPa (Table 2), representing the highest values reported for undoped samples in the literature and obtained via short-duration, high-temperature pre-heat treatments. This trend—in which microhardness values increase with pre-heat treatment temperature—suggests that higher pre-heat treatment temperatures not only mitigate carbon-related limitations but also enhance sintering kinetics and the overall effectiveness of the SPS process.

The influence of boron addition was negligible at lower pre-heat treatment temperatures (650 °C–1 h), where the highly amorphous nature of the samples dominated. At this stage, undoped and 2% B-doped samples exhibited similar hardness values (7.34 and 7.36 GPa), indicating that limited crystallinity and low densification overshadowed the role of B incorporation. In contrast, a clear improvement emerged at 900 °C–15 min, where the 2% B-doped sample (7.88 GPa) showed markedly higher hardness than

the undoped counterpart (7.44 GPa), consistent with improved densification and crystallinity. At 1000 °C, however, while the undoped sample reached the highest hardness (8.05 GPa), increasing B content caused a gradual decline, correlating with reduced density and structural modifications at higher doping levels. Overall, hardness trends paralleled density data, reflecting the strong interplay between phase composition, microstructure, and mechanical performance. Notably, 1% B-doped sample surpassed previously reported hardness values, demonstrating the potential of boron doping to enhance mechanical properties under milder sintering conditions. Yet, excessive B addition negated this benefit, highlighting the need for optimized dopant content to maximize hardness without compromising microstructural integrity.

FESEM images of SPS-treated undoped and B-doped samples after HF treatment are shown in Fig. 11. In undoped samples, the grains appeared more isolated, whereas B doping promoted a more interconnected morphology with a transition from predominantly spherical to ellipsoidal geometries. Consistent with density and hardness analyses, samples pre-heat-treated at 650 °C for 1 h exhibited relatively large grain sizes after sintering (53 and 61 nm for undoped and 2% B-doped, respectively). In contrast, the undoped sample pre-heat-treated at 1000 °C for 5 min, which contained the highest tetragonal phase fraction, showed the smallest average grain size (36 nm), a highly uniform particle size distribution, and the highest hardness among

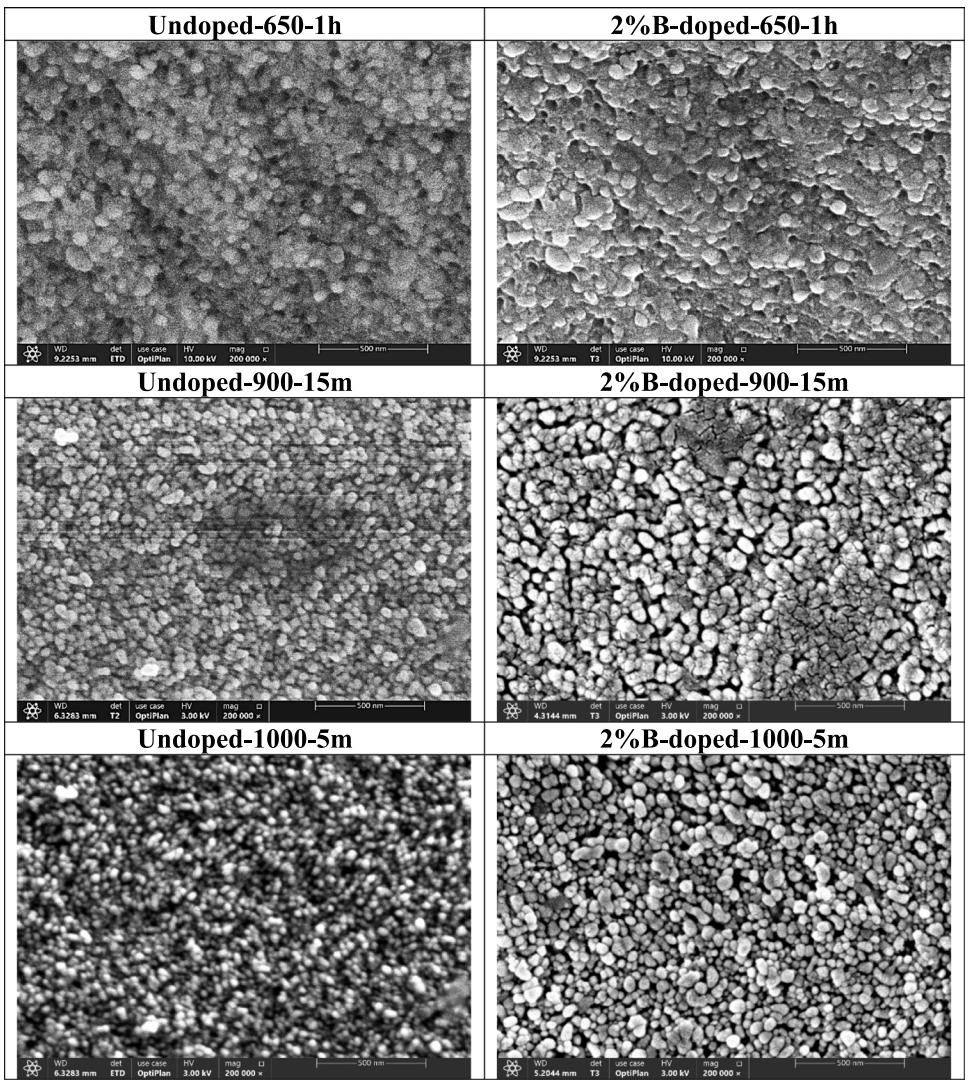


Figure 11 FESEM images of SPS-treated undoped and B-doped samples after HF treatment, illustrating grain morphology evolution and size differences with pre-heat treatment temperature and B incorporation.

all compositions. In agreement with the stabilizing role of boron on the tetragonal phase, B doping significantly increased the final grain size.

Conclusions

This study investigated the influence of boron doping and pre-heat treatment temperature on the densification, microstructure, and mechanical properties of SPS-processed glass–ceramic samples. Boron incorporation had a negligible effect at low pre-heat treatment temperatures (650 °C) due to the highly amorphous nature of the samples, but significantly enhanced densification, crystallinity, and hardness at intermediate conditions (900 °C). At higher temperatures (1000 °C), excessive B addition reduced hardness, correlating with decreased density and grain coarsening. FESEM analysis confirmed that boron promoted interconnected, ellipsoidal grain morphologies and larger grain sizes, consistent with its role in stabilizing the tetragonal phase. Overall, hardness evolution closely followed density trends, highlighting the strong interplay between phase composition, microstructure, and mechanical performance. Importantly, moderate boron doping (≈1%) surpassed previously reported hardness values under milder sintering conditions, whereas excessive levels proved detrimental, emphasizing the need for optimized dopant concentrations to maximize mechanical performance in SPS-derived glass–ceramics. The increased density and hardness of the SPS-treated samples are directly supported by the microstructural features observed in the FESEM images, including reduced porosity and well-densified, interconnected grains. Such microstructural characteristics are critical for mechanical reliability in restorative dentistry applications. While no biological or clinical tests were performed, the observed density, hardness, and controlled tetragonal phase stabilization—achieved through optimized boron doping and pre-heat treatment temperature—demonstrate the mechanical suitability of these SPS-derived glass–ceramics for dental restorations.

Acknowledgements

The authors gratefully acknowledge the Yildiz Technical University Scientific Research Projects Coordination Unit for funding through project FBA-2025-6788. This paper is also submitted in partial fulfillment of the requirements for the Ph.D. degree at Yildiz Technical University.

Author contributions

Yusuf Çelik contributed to investigation, writing—original draft, and validation. Ahmet Furkan Buluç contributed to investigation and validation. Servet Turan contributed to project administration, resources, writing—review and editing. Ali Erçin Ersundu contributed to writing—original draft, writing—review and editing, validation, resources, project administration, and supervision. Miray Çelikbilek Ersundu contributed to conceptualization, writing—original draft, writing—review and editing, validation, visualization, resources, project administration, and supervision.

Funding

Open access funding provided by the Scientific and Technological Research Council of Türkiye (TÜBİTAK). Funding was provided by the Yildiz Teknik Üniversitesi, Grant NO: FBA-2025-6788, Miray Çelikbilek Ersundu

Declarations

Conflict of interest The authors declare that they have no known competing financial interests or personal relationships that could have appeared to influence the work reported in this paper.

Supplementary Information The online version contains supplementary material available at https://doi.org/10.1007/s10853-026-12452-1.

Open Access This article is licensed under a Creative Commons Attribution 4.0 International License, which permits use, sharing, adaptation, distribution and reproduction in any medium or format, as long as you give appropriate credit to the original author(s) and the source, provide a link to the Creative Commons licence, and indicate if changes were made. The images or other third party material in this article are included in the article's Creative Commons licence,

unless indicated otherwise in a credit line to the material. If material is not included in the article's Creative Commons licence and your intended use is not permitted by statutory regulation or exceeds the permitted use, you will need to obtain permission directly from the copyright holder. To view a copy of this licence, visit http://creativecommons.org/licenses/by/4.0/.

References

[1] Skorulska A, Piszko P, Rybak Z, Szymonowicz M, Dobrzyński M (2021) Review on polymer, ceramic and composite materials for CAD/CAM indirect restorations in dentistry—application, mechanical characteristics and comparison. Materials 14:1592. https://doi.org/10.3390/ma14071592

[2] Kelly JR, Benetti P (2011) Ceramic materials in dentistry: historical evolution and current practice. Aust Dent J 56:84–96. https://doi.org/10.1111/j.1834-7819.2010.01299.x

[3] Kelly JR, Denry I (2008) Stabilized zirconia as a structural ceramic: an overview. Dent Mater 24:289–298. https://doi.org/10.1016/j.dental.2007.05.005

[4] Guazzato M, Albakry M, Ringer SP, Swain MV (2004) Strength, fracture toughness and microstructure of a selection of all-ceramic materials. Part II. Zirconia-based dental ceramics. Dent Mater 20:449–456. https://doi.org/10.1016/j.dental.2003.05.002

[5] Zhang Y, Lawn BR (2018) Novel zirconia materials in dentistry. J Dent Res 97:140–147. https://doi.org/10.1177/0022034517737483

[6] Piconi C, Maccauro G (1999) Zirconia as a ceramic biomaterial. Biomaterials 20:1–25. https://doi.org/10.1016/S0142-9612(98)00010-6

[7] Zhang Y, Kim JW (2010) Graded zirconia glass for resistance to veneer fracture. J Dent Res 89:1057–1062. https://doi.org/10.1177/0022034510375289

[8] Chevalier J (2006) What future for zirconia as a biomaterial? Biomaterials 27:535–543. https://doi.org/10.1016/j.biomaterials.2005.07.034

[9] Grossman D (1973) Tetrasilicic mica glass-ceramic method, U.S. Patent No. 3,732,087, U.S. Patent and Trademark Office, Washington, DC.

[10] Primus C, Chu C, Shelby J, Buldrini E, Heckle C (2002) Opalescence of dental porcelain enamels. Quintessence Int 33:439–449

[11] Lara C, Pascual MJ, Durán A (2004) Glass-forming ability, sinterability and thermal properties in the systems RO–BaO–SiO_2 (R = Mg, Zn). J Non-Cryst Solids 348:149–155. https://doi.org/10.1016/j.jnoncrysol.2004.08.140

[12] Fu L, Wu C, Grandfield K, Unosson E, Chang J, Engqvist H, Xia W (2016) Transparent single crystalline ZrO_2–SiO_2 glass nanoceramic sintered by SPS. J Eur Ceram Soc. https://doi.org/10.1016/j.jeurceramsoc.2016.05.016

[13] Fu L, Engqvist H, Xia W (2017) Highly translucent and strong ZrO_2–SiO_2 nanocrystalline glass ceramic prepared by sol–gel method and spark plasma sintering with fine 3D microstructure for dental restoration. J Eur Ceram Soc 37:4067–4081. https://doi.org/10.1016/j.jeurceramsoc.2017.05.039

[14] Wang SW, Huang XX, Guo JK (1996) Wet chemical synthesis of ZrO_2–SiO_2 composite powders. J Eur Ceram Soc 16:1057–1061. https://doi.org/10.1016/0955-2219(96)00035-0

[15] Chandradass J, Han KS, Bae DS (2008) Zirconia- and silica-doped zirconia nanopowders prepared by oxalate processing. J Mater Process Technol 206:315–321. https://doi.org/10.1016/j.jmatprotec.2007.12.034

[16] Aguilar DH, Torres-Gonzalez LC, Torres-Martinez LM, Lopez T, Quintana P (2001) A study of the crystallization of ZrO2 in the sol–gel system: ZrO_2–SiO_2. J Solid State Chem 158:349–357. https://doi.org/10.1006/jssc.2001.9126

[17] Zhan Z (1999) A catalyst-free approach for sol–gel synthesis of highly mixed ZrO_2–SiO_2 oxides. J Non-Cryst Solids. https://doi.org/10.1016/S0022-3093(98)00810-2

[18] Tarafdar A, Panda AB, Pramanik P (2005) Synthesis of ZrO_2–SiO_2 mesocomposite with high ZrO2 content via a novel sol–gel method. Microporous Mesoporous Mater 84:223–228. https://doi.org/10.1016/j.micromeso.2005.05.014

[19] Yang J, Jia D, Li B, Guo Y, Li H, Ma J (2019) Comparison of ZrO_2–SiO_2 sols synthesized by two methods: preparation, stability and physical-chemical structure. Integr Ferroelectr 198:167–178. https://doi.org/10.1080/10584587.2019.1592591

[20] Bannister M (1993) Science and Technology of Zirconia V. CRC Press. https://doi.org/10.1201/9781003421290

[21] Brinker CJ, Scherer GW (1990) Sol–gel science: The physics and chemistry of sol–gel processing. Academic Press, Boston

[22] Livage J, Henry M, Sanchez C (1988) Sol–gel chemistry of transition metal oxides. Prog Solid State Chem 18:259–341. https://doi.org/10.1016/0079-6786(88)90005-2

[23] Innocenzi P (2023) Sol–gel processing for advanced ceramics: a perspective. Open Ceram 16:100477. https://doi.org/10.1016/j.oceram.2023.100477

[24] Sakka S, Kamiya K (1982) The sol–gel transition in the hydrolysis of metal alkoxides in relation to the formation of glass fibers and films. J Non-Cryst Solids 48:31–46. https://doi.org/10.1016/0022-3093(82)90244-7

[25] Klein CS, Hurlbut ND (1993) Manual of Mineralogy, 21st edn. John Wiley, New York, p 527

[26] Fu L, Xia W, Engqvist H, Huang J, Li B (2021) Size-driven phase transformation and microstructure evolution of ZrO_2 nanocrystallites associated with thermal treatments. J Eur Ceram Soc. https://doi.org/10.1016/j.jeurceramsoc.2021.04.058

[27] Fu L, Jiang F, Li B, Cheng Y, Xu G, Huang J, Engqvist H, Xia W (2021) Doping of tantalum, niobium, and hafnium in a translucent ZrO_2–SiO_2 nanocrystalline glass-ceramic. J Eur Ceram Soc. https://doi.org/10.1016/j.jeurceramsoc.2021.12.019

[28] Liu Y, Yang D, Riekehr L, Engqvist H, Fu L, Xia W (2021) Combining good mechanical properties and high translucency in yttrium-doped ZrO_2–SiO_2 nanocrystalline glass-ceramics. J Eur Ceram Soc. https://doi.org/10.1016/j.jeurceramsoc.2021.09.047

[29] Fu L, Wang B, Deng Y, Xu G, Huang J, Engqvist H, Xia W (2022) Liquid-phase sintering of ZrO_2-based nanocrystalline glass–ceramics achieved by multielement co-doping. J Am Ceram Soc. https://doi.org/10.1111/jace.18945

[30] Fu L, Wang B, Song J, Xu C, Xu G, Sun Q, Huang J, Engqvist H, Xia W (2022) Understanding microstructure–mechanical properties relationship in ZrO_2–SiO_2 nanocrystalline glass-ceramics: the effect of ZrO2 content. Mater Sci Eng A 840:142904. https://doi.org/10.1016/j.msea.2022.142904

[31] Li W, Xia Y, Zhang C, Wang J-X, Wang D, Zeng X-F, Chen J-F (2008) Facile synthesis of pure monoclinic and tetragonal zirconia nanoparticles. Langmuir 24:4884–4891. https://doi.org/10.1021/la800370r

[32] Nogami M, Tomozawa M (1986) ZrO_2-transformation-toughened glass-ceramics prepared by the sol–gel process from metal alkoxides. J Am Ceram Soc 69:99–102. https://doi.org/10.1111/j.1151-2916.1986.tb04709.x

[33] Garvie R, Hannink R, Pascoe RT (1975) Ceramic steel. Nature 253:703–704. https://doi.org/10.1038/258703a0

[34] El-Meliegy E, van Noort R (2012) Design of medical glass-ceramics. Springer. pp 109–131. https://doi.org/10.1007/978-1-4614-1228-1_7

[35] Wondraczek L, Dittmar A, Oelgardt C, Celarie F, Ciccotti M, Marliere C (2006) Real-time observation of a non-equilibrium liquid condensate confined at tensile crack tips in oxide glasses. J Am Ceram Soc 89:746–749. https://doi.org/10.1111/j.1551-2916.2005.00765.x

[36] Gomez R, Lopez T, Bokhimi X, Muñoz E, Boldu JL, Novaro O (1998) Dehydroxylation and the crystalline phases in sol–gel zirconia. J Sol-Gel Sci Technol 11:309–319. https://doi.org/10.1023/A:1008666531404

[37] Becher P, Swain M (1992) Grain-size-dependent transformation behavior in polycrystalline tetragonal zirconia ceramics. J Am Ceram Soc 75:493–502. https://doi.org/10.1111/j.1151-2916.1992.tb07832.x

[38] Ponnilavan V, Vasanthavel S, Singh RK, Kannan S (2015) Influence of La^{3+} additions on the phase behaviour and antibacterial properties of ZrO_2–SiO_2 binary oxides. Ceram Int 41:7632–7639. https://doi.org/10.1016/j.ceramint.2015.02.089

[39] Chu H, Xu M, Liu B, Pan Z, Pan H, Zhao S, Xu D, Li D (2024) Fabrication of amorphous nanoporous ZrO_2/SiO_2 aerogel enabling nonlinear optical properties. J Materiomics 10:1109–1116. https://doi.org/10.1016/j.jmat.2023.11.014

[40] Liu Y, Yang J (2022) Hydrophobic modification of ZrO_2–SiO_2 xerogel and its adsorption properties to rhodamine B. Gels 8:675. https://doi.org/10.3390/gels8100675

[41] Kongwudthiti S, Praserthdam P, Tanakulrungsank W, Inoue M (2003) The influence of Si–O–Zr bonds on the crystal-growth inhibition of zirconia prepared by the glycothermal method. J Mater Process Technol 136:186–189. https://doi.org/10.1016/S0924-0136(03)00157-2

[42] Lian M, Wang T, Wei C (2024) Effect of B_2O_3 and basic oxides on network structure and chemical stability of borosilicate glass. Ceramics 7:516–529. https://doi.org/10.3390/ceramics7020034

[43] Fu L, Li L, Cheng Y, Wang B, Wu H (2022) Influences of powder morphology on the densification and microstructure of a ZrO_2-based nanocrystalline glass–ceramic. J Am Ceram Soc. https://doi.org/10.1111/jace.18767

Publisher's Note Springer Nature remains neutral with regard to jurisdictional claims in published maps and institutional affiliations.